Interpretation of the JANUS Phase 7 shielding experiment with TRIPOLI-4® and quantification of uncertainties due to nuclear data

Amine Hajji, Christine Coquelet-Pascal, Patrick Blaise

Version of Record: https://www.sciencedirect.com/science/article/pii/S0306454920304746
Manuscript_1563ec5b472831958b15ea0274f071b5

Interpretation of the JANUS Phase 7 shielding experiment with TRIPOLI-4® and quantification of uncertainties due to nuclear data

Amine Hajji[a1], Christine Coquelet-Pascal[b], Patrick Blaise[b]

a: CEA Cadarache, DES/IRESNE/DER/SPRC/LE2C, F-13108 Saint Paul Lez Durance, France

b: CEA Cadarache, DES/IRESNE/DER/SPESI, F-13108 Saint Paul Lez Durance, France

Abstract: The JANUS Phase 7 shielding experiment performed in the NESTOR experimental reactor in 1991 studied deep fast neutron propagation in mild steel, boron carbide and sodium. Several steel plates, followed by boxes containing boron carbide and sodium were used as neutron shielding next to a fission plate. Gold, manganese, rhodium and sulphur detectors were positioned at several depths in order to measure the neutron flux at different energies. This experiment is interpreted using the Monte-Carlo code TRIPOLI-4® and different nuclear data for iron 56 and sodium. C/E results exhibit discrepancies generally smaller than 10 % for the gold detector, while larger discrepancies are obtained for the sulphur detector. In order to understand the obtained biases, sensitivity calculations were performed to compute the uncertainties on the detector responses due to nuclear data. We show that the propagated uncertainties may explain a large part of the observed discrepancies.

1. Introduction

Neutron shielding plays an important role in fast reactors [1] as neutrons leaking from the core may have several consequences on the performance, cost and lifetime of the reactor: they can activate the sodium in the secondary loop, leading to more difficult maintenance operations and decreasing the effective availability of the reactor. They also lead to neutron damage on the vessel and the structures, leading to limitations on the reactor's lifetime. In order to mitigate these effects, it is necessary to have efficient and reliable neutron shielding.

Historically, steel has been used almost universally as neutron shielding in past and present fast reactors. However, even if this material has excellent mechanical properties, a relatively low cost, and is somewhat efficient as neutron shielding, it may lead to large shielding thickness as it is mainly a neutron reflector, which is able to reflect a large proportion toward the core but with a small ability to capture fast neutrons. This may lead to large and therefore costly reactor vessels. As a result, more efficient materials, possibly neutron absorbers, become interesting as neutron shielding for future reactors.

One of such materials is boron carbide, which is commonly used as an absorber in safety systems such as control rods. In order to validate neutron calculations with this material, experiments are needed as part of the V&V&UQ (Verification, Validation and Uncertainty Quantification) procedure.

As part of the European cooperation for the design of the EFR (European Fast Reactor), the JANUS shielding programme [1][2] studied neutron shielding in fast reactors. It was performed on the ASPIS shielding facility of the NESTOR reactor at Winfrith, United Kingdom during the late 1980's and early 1990's. This set of experiments focused on neutron propagation and shielding in several materials considered for fast reactor applications such as different kinds of steel, boron carbide and sodium. One of these experiments featuring mild steel (> 99 % iron) has been interpreted in the article [4]. The 7th phase of these experiments treats neutron propagation in mild steel, boron carbide and

[1] amine.hajji@cea.fr

sodium, a configuration that could be representative of neutron shielding in future fast reactors. This experiment has already been interpreted in the early 1990's using nowadays obsolete nuclear data libraries (JEF-1, UKNDL) and old deterministic (CCRR) and Monte-Carlo (MCBEND) codes [2]. It is therefore interesting to check whether the performance and accuracy of the calculations be increased with current nuclear data and methods.

The studies presented in this article aim to check if current reference calculation tools as well as state-of-the-art evaluated nuclear data libraries are able to reproduce the experimental results within their experimental uncertainties. Moreover, these studies were performed to identify potential sources of residual biases due to inconsistent nuclear data. A complete sensitivity and uncertainty analysis completes the work, and proposes improvement in nuclear data libraries to reduce biases and uncertainties on the design of neutron shielding using similar configurations.

2. The NESTOR Facility and the JANUS Phase 7 experiment

NESTOR is a 30 kW research nuclear reactor cooled with light water and moderated with both light water and graphite, located at Winfrith, United Kingdom. The reactor is surrounded by a graphite reflector/moderator and several experimental facilities. One of these facilities consists in a cavity that contains the so-called "ASPIS" trolley. The aim of this facility is to simulate neutron shielding: it contains a fission plate followed by the shielding studied during the experiment.

The fission plate uses a metallic uranium-aluminium alloy, with a very high uranium 235 enrichment (93 %). Neutrons leaking from the core induce fissions inside the fission plate. Then, the emitted fission neutrons propagate inside the shielding. A description of the NESTOR reactor and the ASPIS facility [3] is depicted in Figure 1.

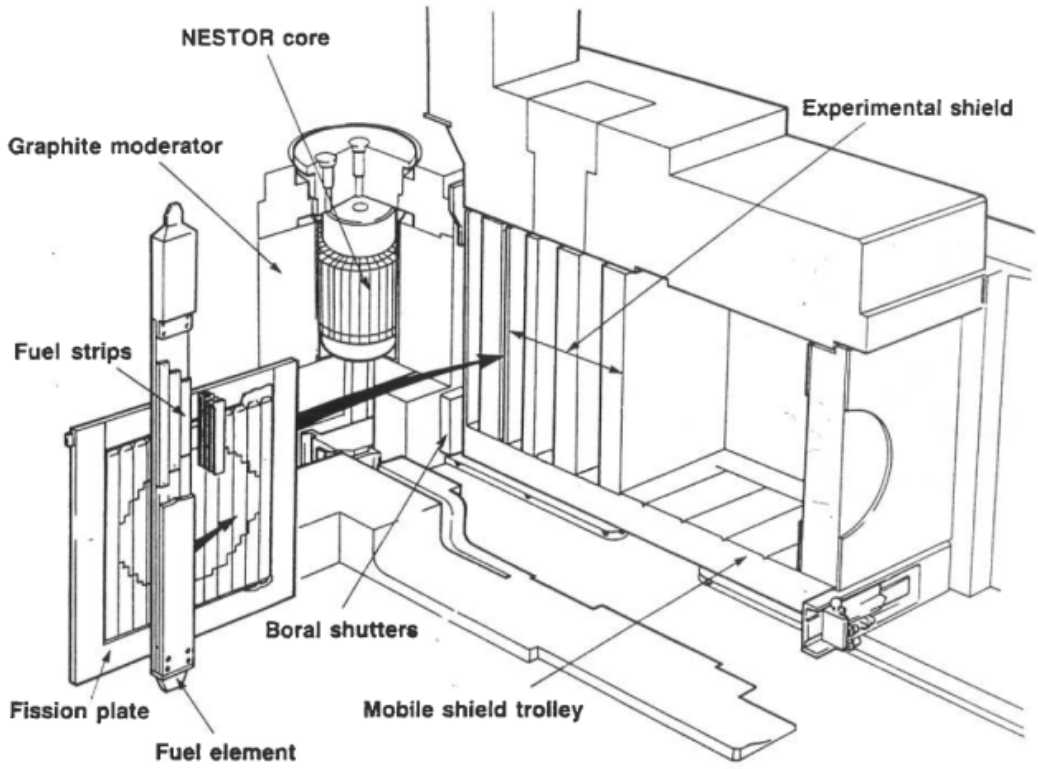

Figure 1. The NESTOR reactor with the APSIS experimental facility [3]

The JANUS Programme aims to simulate neutron propagation in materials typical of those encountered in fast reactors neutron shielding, including mild steel (> 99 % iron), stainless steel (steel containing various concentrations of chromium, nickel, manganese, molybdenum next to iron), sodium and boron carbide. The JANUS Phase 7 experiment treats neutron propagation first in mild steel, then in boron carbide and finally in sodium as shown in Figure 2.

First, four layers of mild steel (99.02 % iron, 0.74 % manganese and 0.23 % carbon) which are 1.8 m wide and 1.9 m high, with a total thickness of about 18 cm, are positioned next to the fission plate. Then, several steel boxes containing boron carbide are placed in a complex framework in order to fill the ASPIS cavity with an effective thickness of about 50 cm. Then, sodium filled boxes are positioned to fill the cavity with a total sodium thickness about 90 cm. The disposition of the steel plates and boron carbide and sodium boxes allows putting activation detectors between two consecutive plates/boxes at the centre line of the fission plate.

There are four types of activation detectors used during the experiment in order to measure the neutron flux in different energy ranges. Their specifications are presented in Table 1 The associated activation reaction cross sections are detailed in Figure 3.

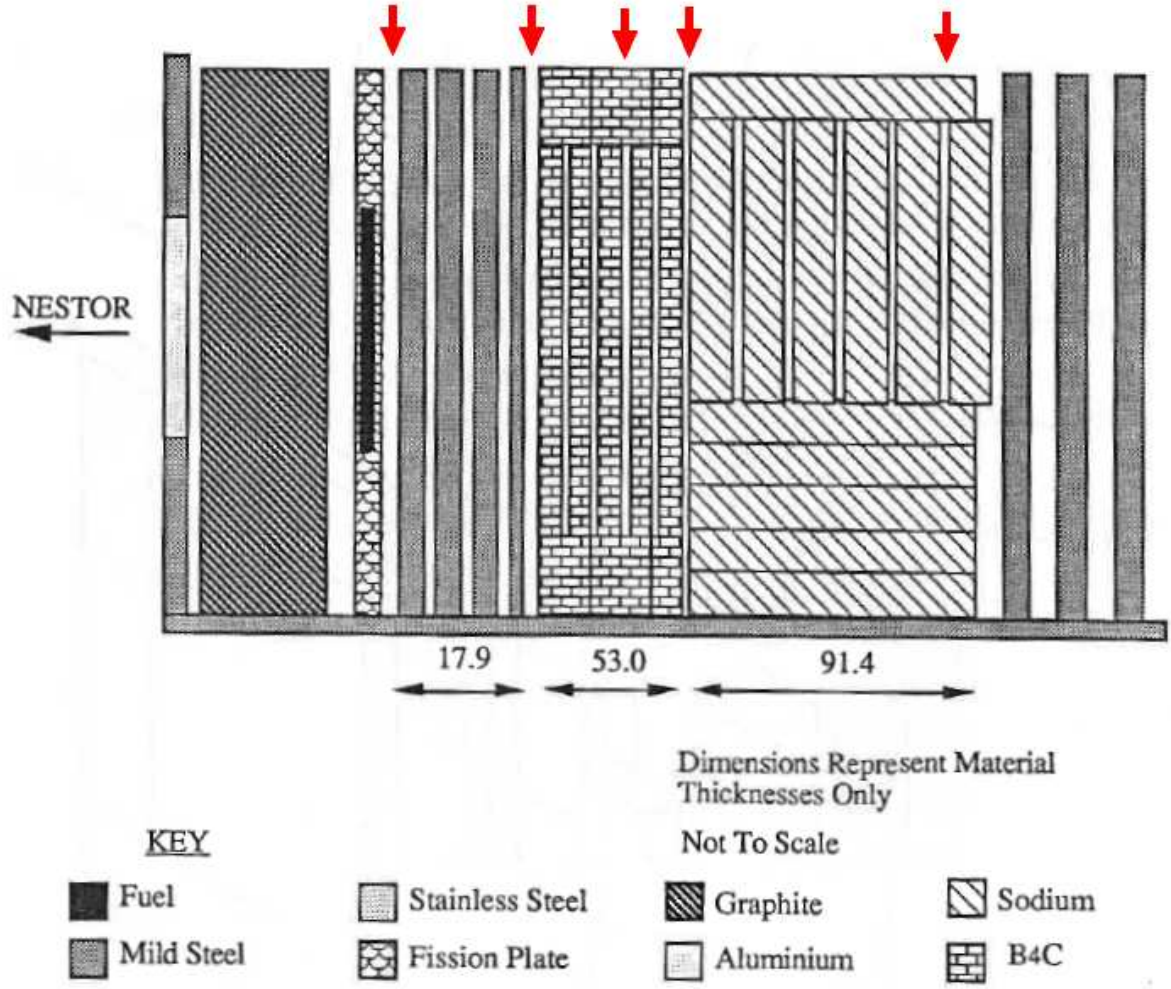

Figure 2. Description of the JANUS Phase 7 experiment [3], red arrows show the positions where the neutron spectra are calculated

Detector[2]	Diameter	Thickness	Cadmium	Calibration uncertainty(3)	Counting uncertainty	Reaction threshold
$^{197}Au(n,\gamma)^{198}Au$	12.7 mm	0.05 mm	1.27mm(4)	0.9 %	~ 1 %	-
$^{55}Mn(n,\gamma)^{56}Mn$	12.7 mm	0.15 mm	1.27 mm	1.5 %	~ 1 %	-
$^{103}Rh(n,n')^{103m}Rh$	12.7 mm	0.015 mm(5)	-	3 %	1-2 %	40 keV
$^{32}S(n,p)^{32}P$ (6)	51 mm	5.6 mm	-	5 %	1-20 %	900 keV

[2] The composition of the detectors was assumed to be pure with the natural isotopic composition as no precisions were given about their exact composition, with the exception of the manganese detector. For the latter, the JANUS handbook [3] states that it contains some nickel, but the actual proportion was not provided. Therefore, the proportion used is that the one found in an interpretation of the JANUS Phase 1 experiment [4] (88 % manganese, 12 % nickel).

[3] As no precisions whether these are 1σ or 2σ uncertainties, it has been assumed that these were 1σ uncertainties, as found in a previous interpretation of the ASPIS Iron 88 experiment in the same experimental facility. [6].

[4] There are no information whether it corresponds to the total thickness of the cadmium cover or to the thickness for each side of the detector. The impact has been proved to be limited (Figure A 7 in appendix). We therefore assumed this value to be the total thickness of the cadmium cover.

[5] The provided value seems weird as the 0.2g mass would give an unrealistic density of 105 g/cm^3. In addition, the Winfrith Iron experiment [7], part of the SINBAD database [6] uses a thickness of 0.25 mm, which is more compatible with the mass of the detector. A study, presented in Figure A 9, shows that the impact is negligible. Therefore, the original 0.015 mm thickness was kept.

Table 1. Detectors used in the JANUS Phase 7 benchmark

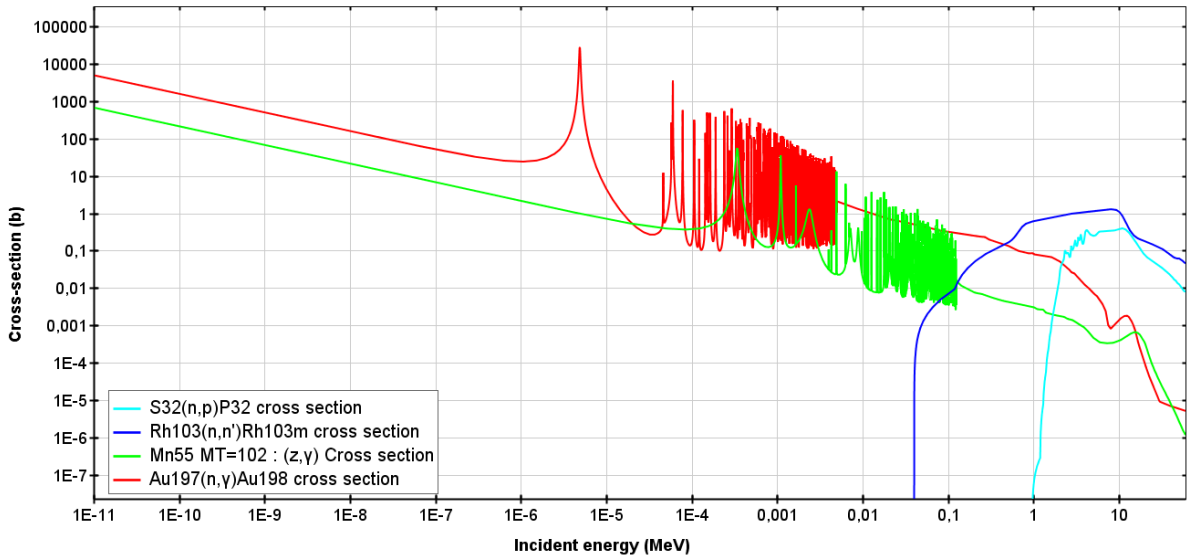

Figure 3. Cross sections of the activation reactions of each detector (IRDFF-1.05 evaluation)

The principle of the experiment is as follows: neutrons leaking form the NESTOR core enter the experimental facility and cause fissions inside the fission plate. The subsequent fission neutrons propagate in the shielding facility and activate the detectors. The fission source of the plate is determined using sulphur and manganese detectors as well as the combustion rate of the plate. This fission source is presented in Figure 6. Note that the uncertainty on the power of the fission plate is 4 %, as this power may slightly vary from an experiment to another.

This calibration process allows to calculate *absolute* reactions rates, as it avoids normalising C/E ratios to 1 as in other similar experiments. However, there are still neutrons leaking from the NESTOR core that are able to induce reactions in the detectors. The contribution of these neutrons is evaluated by doing the measurements with and without the fission plate, the latter measurement gives the contribution of the NESTOR neutrons. The induced contribution is important for gold and manganese detectors, with more than 30 % of the reaction rate of the first gold detector position coming from the leaking NESTOR neutrons. Therefore, this contribution is subtracted from the total reaction rate. For the sulphur and rhodium threshold detectors, this contribution can be neglected, as the neutrons leaking from the NESTOR core are mainly thermal.

The following figure reproduces the measured reaction rate profiles.

[6] The experimental data [3] also feature a smaller detector with a 38.1 mm diameter and 2.41 mm thickness. It has been proved (Figure A 10) that the impact was negligible. The larger detector has therefore been used in the interpretation.

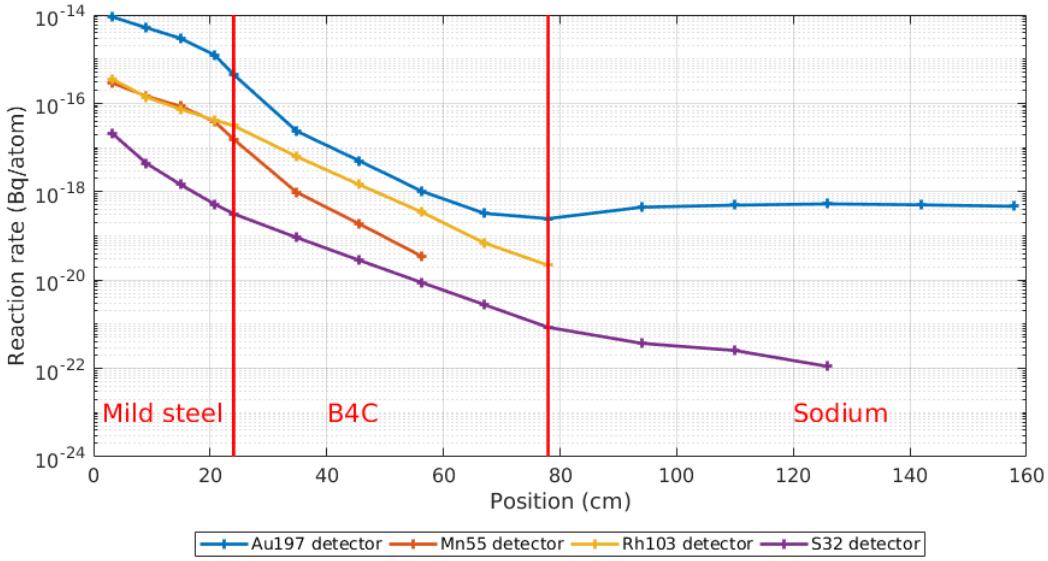

Figure 4. Reaction rates obtained during the JANUS Phase 7 experiment for each detector

Figure 4 shows that reaction rates behave differently with the nature of the detector. For example, the gold reaction rate decreases much faster in boron carbide than in steel or in sodium (it even slightly increases at the beginning of the sodium zone). This is due to the fact that this detector uses an epi-thermal reaction, while boron carbide is an efficient absorber for thermal and epi-thermal neutrons. The slight increase in sodium can be explained by neutrons slowing down in this material, leading to more epi-thermal reactions. Meanwhile, for the sulphur detector, the reaction rate decreases much more quickly than for the gold detector (6 decades in 120 cm in comparison to 4 decades), but the decrease rate is not higher in boron carbide than in steel: if boron carbide is a very efficient shield for thermal neutrons, it is much less efficient for fast neutrons.

3. Comparison between TRIPOLI-4® and the experiment

In this part, the calculation over experiment (C/E) ratios obtained for the JANUS Phase 7 experiment are presented. Statistical uncertainties are given at 1σ on the figures. First, the TRIPOLI-4® model for the experiment is presented. An analysis of the uncertainties due to nuclear data is performed in the following part.

3.1. TRIPOLI-4® benchmark modelling

The general multi-purpose Monte-Carlo code TRIPOLI-4®[8] is used to interpret the JANUS Phase 7 experiment. The ASPIS experimental facility is described in three dimensions in the input file. However, as the description of the NESTOR core was not provided in the experimental data handbook, an assumption is needed to take into consideration neutrons reflected by the graphite reflector of the NESTOR reactor back into the experimental facility. Therefore, a 50 cm thick graphite reflector was added before the experimental facility, as shown in Figure 5. Similar assumptions were made during the interpretation of other experiments on the same experimental facility [4][9]. The lack of precision of some of the experimental data made this assumption, as well as some other assumptions on the size of the detector, necessary for this study. Their impact is presented in **Figure A** 7 to **Figure A** 10 in the appendix.

The detectors were modelled explicitly with their actual dimensions presented on Table 1. For the gold and manganese detectors, the cadmium cover was also modelled. The fission source provided in the experimental data (Figure 6) is introduced into the calculation as an external source, with the thermal fission spectrum of uranium 235. Multiplication of the fission source inside the fission plate is not considered. Variance reduction techniques are used to speed up the convergence of the calculations. For threshold detectors, tracked neutrons are killed when they slowed down under the threshold energy, as there is no up-scattering at these energies. The track length estimator is used because it has better computational performances than the collision estimator for the threshold detectors.

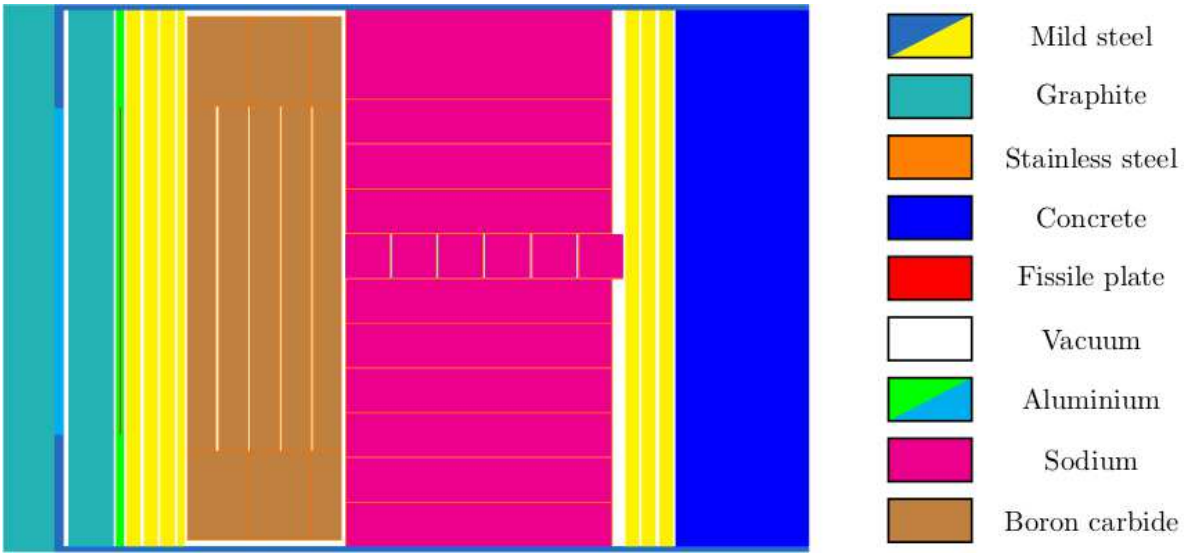

Figure 5. Upper view of the TRIPOLI-4® modelling of the JANUS Phase 7 experiment based on the experimental data [3], note the added graphite zone on the left

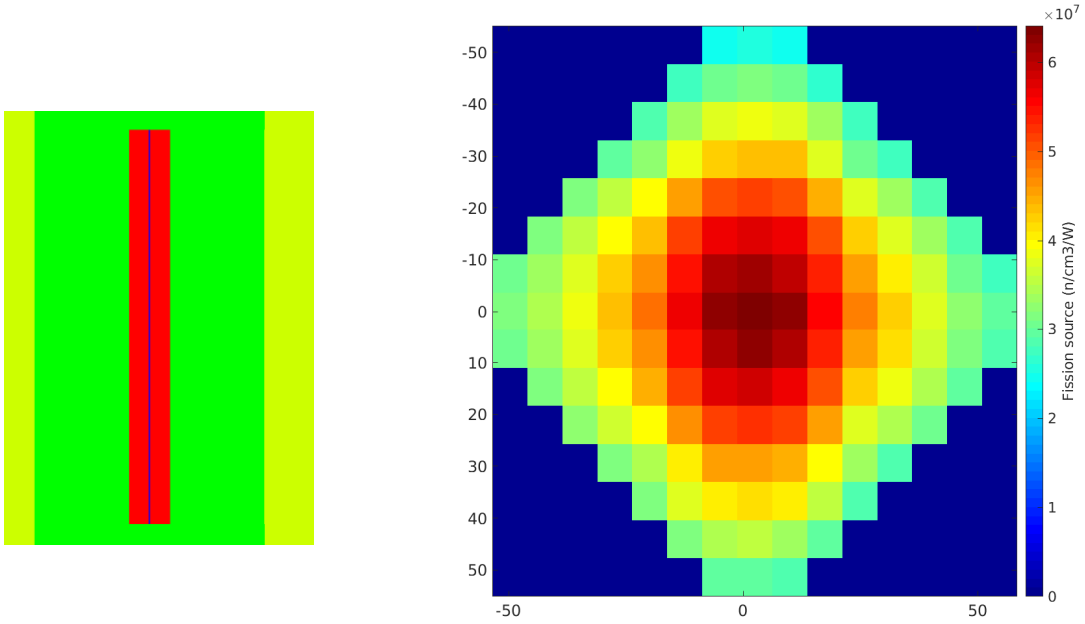

Figure 6. Model of the gold detector (blue) with its cadmium cover (red) in the TRIPOLI-4® calculation based on the data of Table 1 (left), geometric distribution of the fission source on the fissile plate [3] (right)

Neutron transport calculations are performed with the JEFF-3.1.1 [10] and the JEFF-3.2 [11] nuclear data libraries. Furthermore, additional calculations were done with the JEFF-3.2 nuclear data library, replacing the iron 56 evaluation with that of ENDF/B-VIII.0 [12]. The latter evaluation is characterised by higher radiative capture (Figure A 2) and inelastic scattering (Figure A 1) cross sections. For the activation calculation at the detector, the IRDFF-1.05 [13] library is used. Note that, regardless of the library used for activation, the neutron transport calculation in the detector is made with the general-purpose library (JEFF-3.1.1 or JEFF-3.2).

For clarity and to highlight the main phenomena, only the results obtained with the gold (thermal) detector and the sulphur (fast) detector are presented in this document, as there are less measured values with the two other detectors (manganese and rhodium).

3.2. Calculated neutron spectra

In this part, the neutron spectra calculated by TRIPOLI-4® using the JEFF-3.1.1 nuclear data library at the positions shown by the red arrows in Figure 2 using the ECCO 33-group energy mesh [14] are presented. The statistical convergence on the main energy groups is less than 1 %.

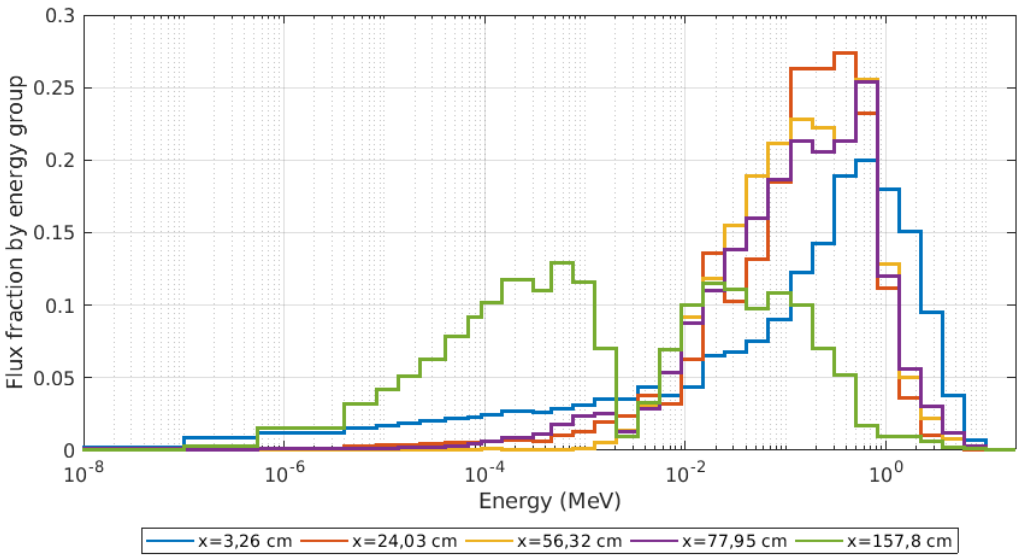

Figure 7. Evolution of the neutron spectrum during propagation (normalised to 1)

Figure 7 shows that, at the beginning of the propagation, the neutron spectrum has a large fast component because of fission neutrons, but also a non-negligible thermal component due to neutrons thermalized and reflected by the graphite zone. In the middle of the boron carbide zone (x=56.32 cm), the neutron flux is faster than in the middle of the steel zone (x=24.03 cm). This can be explained by the nature of boron carbide as a thermal neutron absorber. In the sodium zone (x=157.8 cm), there is an important component for the flux below 1 keV. This is due to the sodium being a light isotope with a low neutron capture cross section. A pit can be seen in the neutron spectrum around 3 keV, which is due to the large sodium resonance in that energy zone. The figure indicates that different phenomena happen in the three successive zones, which may impact the measured and calculated reaction rates.

3.3. Gold detector

In this part, a comparison is made between the reaction rates calculated by TRIPOLI-4® and the experimental results for the gold detector. Both the experimental and the statistical (represented by vertical bars on the plots) uncertainties are given at one standard deviation. The IRDFF-1.05 evaluation is used for activation in both detectors.

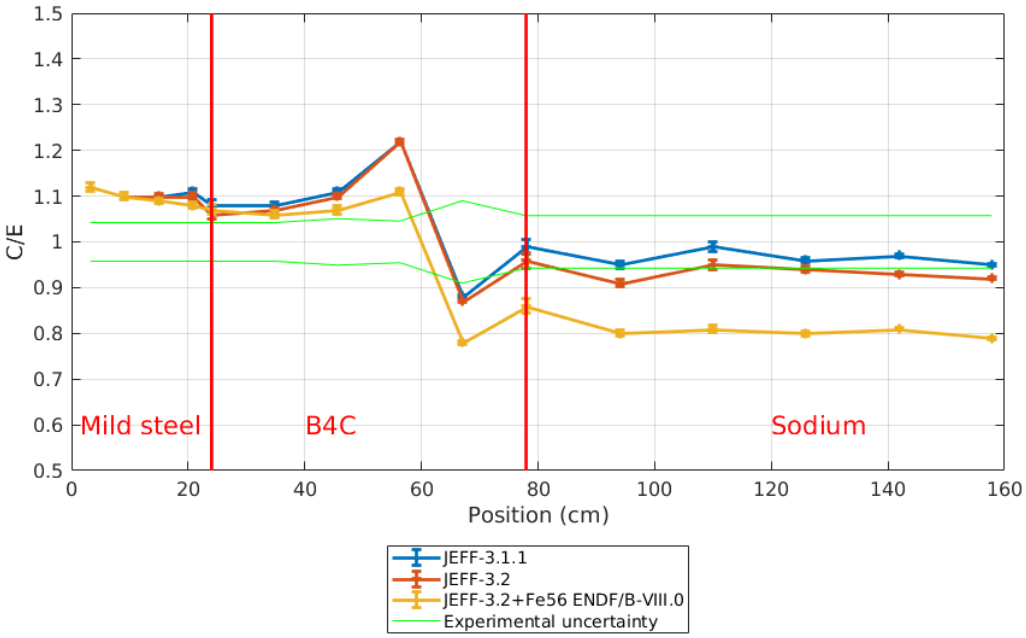

Figure 8. Comparison between the calculated and measured reaction rates for the gold detector

Figure 8 shows that, at the beginning of the neutron propagation, an overestimation of the reaction rates of about 10 % is observed. This overestimation can be explained by either the uncertainty on the power of the fission plate, which is 4% at 1σ, or by the evaluation used for the gold detector, as another evaluation, EAF-2010 [15], gives lower reaction rates, as shown in Figure A 3 in the appendix. In the boron carbide zone, there is an increase in the overestimation tendency up to + 20 % with JEFF-3.1.1 and JEFF-3.2, then a brutal transition to an underestimation behaviour of – 10 % with these two evaluations. Finally, in the sodium zone, the C/E ratios remain almost constant around 0.95. The ENDF/B-VIII.0 evaluation for iron 56 gives lower C/E ratios starting from the middle of the boron carbide zone. This can be explained by the fact that boron carbide absorbs slow neutrons and therefore neutrons propagating deep in this material are mainly fast, which can be affected by the change in the inelastic scattering cross section introduced by the ENDF/B-VIII.0 evaluation. Note that iron 56 is present not only in the mild steel zone but also in the boxes containing sodium and boron carbide. The observed trend on the C/E using ENDF/B-VIII.0 evaluation has also been obtained in our previous study of the Iron-88 benchmark [4].

The gold detector is commonly used to measure the thermal and epi-thermal neutron flux. However, in boron carbide, there is almost no thermal neutrons and therefore most of the reaction rate occurs at energies higher than 1 keV as seen in Figure 12. This can explain the behaviour observed in the boron carbide zone.

3.4. Sulphur detector

In this part, a comparison is made between the calculated by TRIPOLI-4® and measured reaction rates.

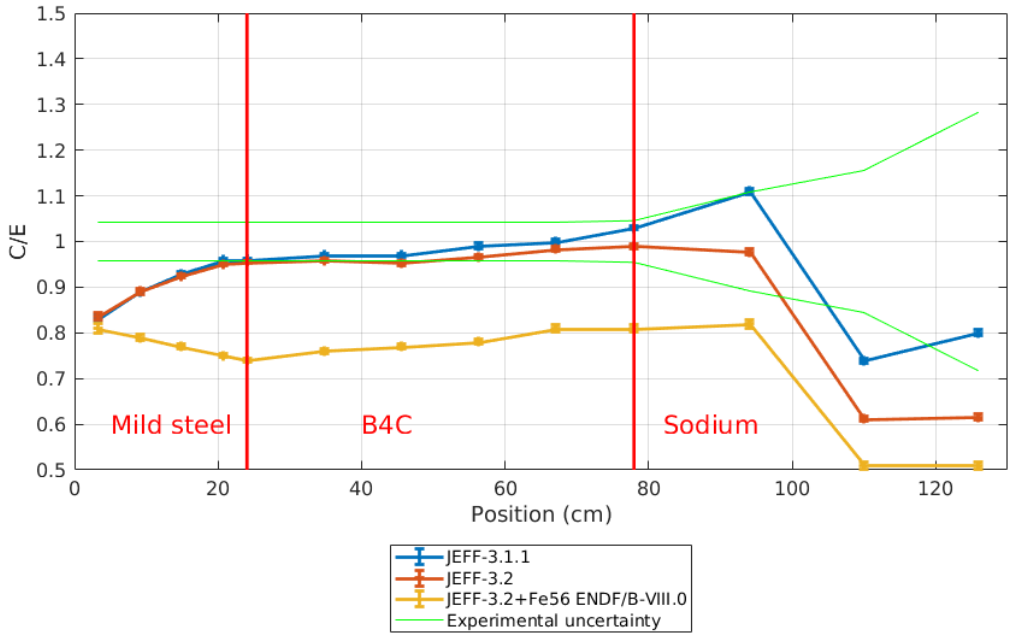

Figure 9. Comparison between the calculated and measured reaction rates for the sulphur detector

Figure 9 shows that at the beginning of the neutron propagation there is an underestimation around -20 % of the reaction rate. Such a behaviour, that looks like a systematics, has also been observed on the ASPIS Iron 88 experiment [4]. It can be explained by several factors, such as not taking neutron multiplication in the fission plate into account, or the detector cross section evaluation. In the mild steel zone, the C/E increases with both JEFF-3.1.1 and JEFF-3.2 evaluations and becomes close to 1, while it further decreases with ENDF/B-VIII.0. The JEFF-3.1.1 and JEFF-3.2 are very similar and even identical for most isotopes in the mild steel with the notable exception of manganese 55. The tendency observed with ENDF/B-VIII.0 is due to the higher inelastic scattering cross section of iron 56.

In the boron carbide zone, the C/E remains almost constant, as boron carbide is mainly a thermal neutron absorber while neutrons that contribute to the reaction rate in the sulphur detector are above 900 keV. Finally, in the sodium zone, the JEFF-3.1.1 evaluation gives higher reaction rates than JEFF-3.2 due to the different sodium evaluation. All evaluations exhibit the same trend: a steep descent, followed by an asymptote far in the sodium zone.

3.5. Preliminary conclusions from C/E comparisons

The interpretation of the JANUS Phase 7 experiment with TRIPOLI-4® shows a different behaviour for (thermal) gold and (fast) sulphur detectors. For the gold detector, the larger C/E discrepancies are obtained inside the boron carbide zone, which can be explained by the fact that this detector is commonly used for thermal neutrons, which are almost inexistent in boron carbide. For the sulphur detector, the larger C/E discrepancies are obtained in the steel and sodium zones, as boron carbide has a small effect on fast neutrons.

In order to fully understand the obtained biases, additional sensitivity calculations to nuclear data need to be performed.

4. Sensitivity calculations

The comparison between the reaction rates calculated by TRIPOLI-4® and those measured during the JANUS Phase 7 experiment give biases that may reach 20%. In order to understand these biases, sensitivity calculations are performed. The sensitivity of the studied reaction rates [16] can approximately be expressed as follows:

$$d(\sigma\Phi) = \Phi d\sigma + \sigma d\Phi$$

The first term of the right hand side is called the direct term, since it is due to the variation of the cross section of the studied detector (in our case, gold and sulphur cross sections). This term is relatively simple to compute, as only the reaction rate by energy group are needed. The second term is called the indirect term as it results from the flux variation due to the variation of all other cross sections composing the JANUS structure. This term may require advanced tools to be computed.

In this part, only the indirect term is studied. Sensitivity calculations are performed using the correlated sampling method implemented in TRIPOLI-4®[16]. This method simulates the trajectory of neutrons as in an unperturbed simulation, but stores variations in the weight of particles for each perturbation. Using these perturbed particle weights, the impact of the perturbation on the calculated value can be computed. This study enables to sort the most important cross sections for this shielding benchmark.

For each detector, the 1-group sensitivities for the elastic scattering, inelastic scattering and capture cross sections are computed for each isotope contained in the shielding (the four isotopes of iron, manganese, carbon, sodium and the two isotopes of boron) during propagation. All calculations are made with the JEFF3.1.1 evaluation.

4.1. Gold detector

The maximum 1-group sensitivities integrated over the whole energy domain calculated during the whole propagation are presented in the table below:

Isotope	Reaction	Maximum absolute value of 1-group sensitivity (%/%)
Iron 56	Elastic scattering Inelastic scattering Capture	0.71 1.08 0.56
Iron 54	Elastic scattering Inelastic scattering Capture	0.17 0.06 0.04
Iron 57	Elastic scattering Inelastic scattering Capture	0.08 0.05 0.02
Manganese 55	Elastic scattering Inelastic scattering Capture	0.11 0.01 0.06
Carbon	Elastic scattering Inelastic scattering Capture	1.14 0.01 $9\ 10^{-4}$

Boron 10	Elastic scattering Inelastic scattering Capture	0.88 $8\ 10^{-3}$ 1.87
Boron 11	Elastic scattering Inelastic scattering Capture	3.29 0.02 $1\ 10^{-4}$
Sodium 23	Elastic scattering Inelastic scattering Capture	1.99 0.03 0.17

Table 2. Maximum absolute sensitivities of the reaction rate for the gold detector

Table 2 shows that the most important sensitivities are related to the scattering properties of the most abundant isotopes in the geometry, such as iron 56, sodium 23, boron 11, and carbon. Only boron 10 presents an important capture component. Figure 10 reproduces the evolution of sensitivities whose maximum value is above 0.15 %/%. Vertical bars represent the statistical uncertainty on the calculated 1-group sensitivities.

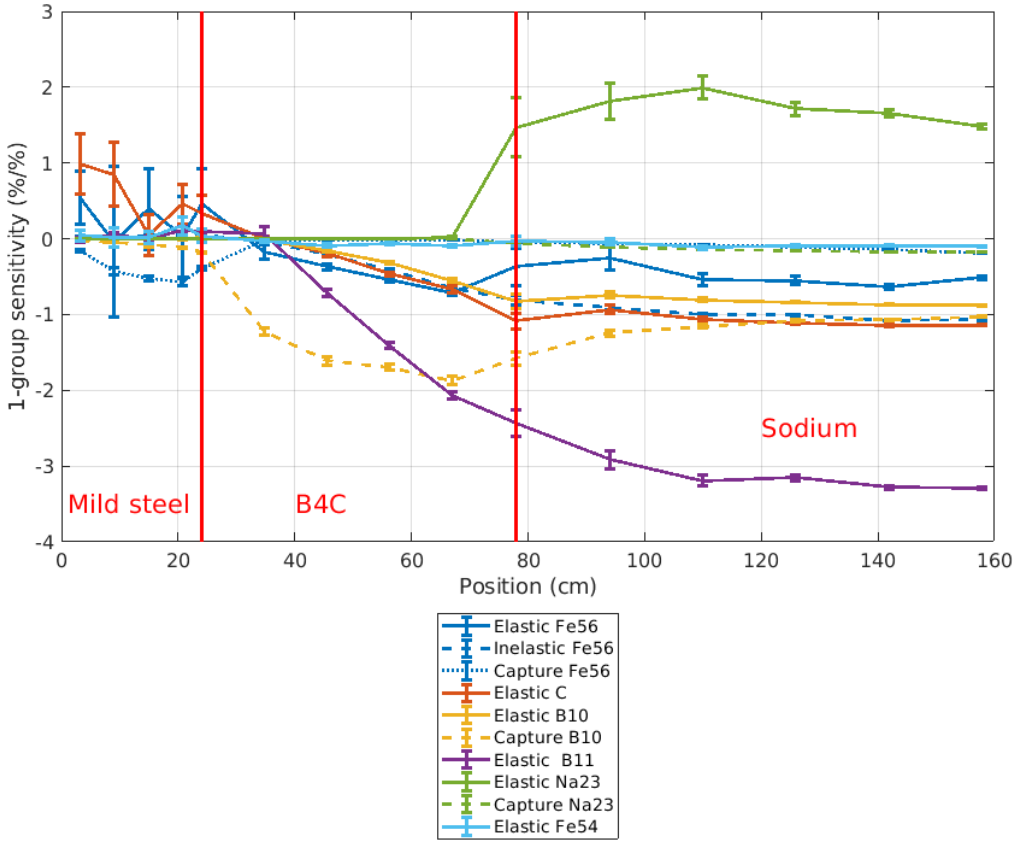

Figure 10. Evolution of 1-group sensitivities for the gold detector

Figure 10 shows that, in the steel zone, the most important sensitivities are those of iron 56 and carbon. The latter isotope is present in steel, boron carbide and graphite. However, its concentration in steel is low (<1%) and therefore this effect is probably due to reflection in boron carbide and graphite. In the boron carbide region, the sensitivities to the elastic scattering of boron 11 and capture of boron 10 become dominant. Finally, in the sodium zone, the sensitivity to the elastic scattering cross section of sodium 23 becomes one of the most important sensitivities. While the sensitivity to the capture

cross section of boron 10 is negative because this reaction reduces the number of neutrons that may interact with the detector, the sensitivity to the elastic scattering depends on the zone and the isotope. For example, the sensitivity to the elastic scattering of boron 11 is negative because this reaction increases the reflection of neutrons before the detector and slows them down, increasing their capture probability in the boron carbide zone. Meanwhile, the sensitivity to the elastic scattering of sodium 23 is positive, because this reaction increases the reflection of neutron after the detector and slows them down, increasing their probability of interaction with the detector.

4.2. Sulphur detector

Isotope	Reaction	Maximum absolute value of 1-group sensitivity (%/%)
Iron 56	Elastic scattering Inelastic scattering Capture	0.84 2.52 0.04
Iron 54	Elastic scattering Inelastic scattering Capture	0.06 0.13 0.05
Iron 57	Elastic scattering Inelastic scattering Capture	0.02 0.07 $6\ 10^{-4}$
Manganese 55	Elastic scattering Inelastic scattering Capture	0.01 0.02 $5\ 10^{-5}$
Carbon	Elastic scattering Inelastic scattering Capture	0.75 0.09 0.01
Boron 10	Elastic scattering Inelastic scattering Capture	0.43 0.09 0.19
Boron 11	Elastic scattering Inelastic scattering Capture	2.21 0.53 $2\ 10^{-3}$
Sodium 23	Elastic scattering Inelastic scattering Capture	0.55 0.66 0.02

Table 3. Maximum absolute sensitivities of the reaction rate for the sulphur detector

Table 3 shows that, once again, the most important sensitivities are related to the most abundant isotopes. However, for the sulphur detector, the sensitivities to the capture cross sections are lower than for the gold case, while the sensitivities to the inelastic scattering cross sections are much higher. Capture is usually higher for low energies while inelastic scattering is a threshold reaction, which explains this behaviour for a threshold detector.

The most important sensitivities are plotted in Figure 11:

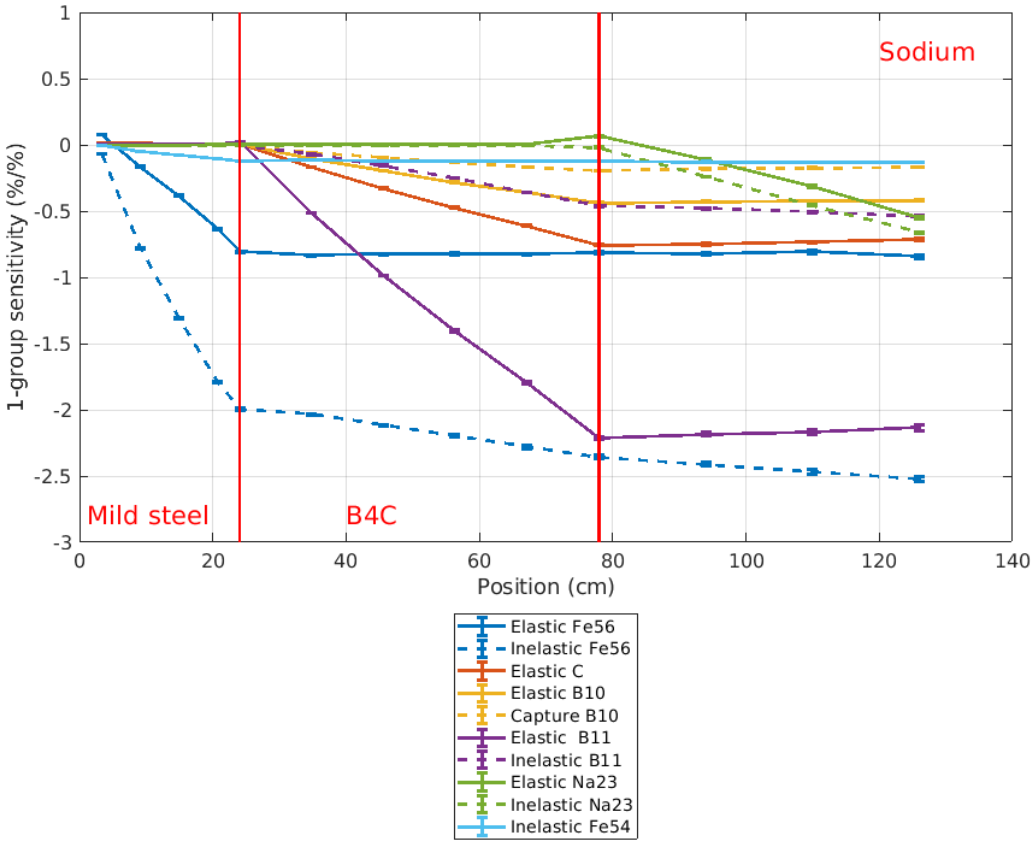

Figure 11. Evolution of 1-group sensitivities for the sulphur detector.

Figure 11 shows that the obtained sensitivities are almost always negative, as opposed to the gold detector where some sensitivities such as the sensitivity to the sodium 23 elastic scattering cross section was positive. The sulphur being a threshold reaction detector, all aforementioned reactions (capture or elastic/inelastic scattering) tend to either reduce or slow down the remaining neutron population below the sulphur threshold energy, hence reducing its response. The absolute values of the obtained sensitivities are smaller than those obtained for the gold detector, as perturbations below the energy threshold of the reaction have no effect for the sulphur detector.

4.3. Conclusions for sensitivity calculations

Indirect sensitivity calculations performed with the TRIPOLI-4® code show that the reaction rates are naturally more sensitive to isotopes that are abundant in the geometry. However, we showed that the most sensitive reactions may change with the detector response: for the gold detector (and for thermal detectors in general), the most sensitive reactions are usually elastic scattering and capture, while for the sulphur detector (and for fast detectors in general), the most sensitive reactions are elastic and inelastic scattering, mainly always negative.

Sensitivity calculations enable to perform quantitative uncertainty propagation calculations on the various detector responses. The uncertainty analysis points out if observed C/E discrepancies can be explained or covered – at least partially – by the nuclear data uncertainties.

5. Uncertainties to nuclear data

In this part, the uncertainties due to nuclear data are computed for the calculated reaction rates of the JANUS Phase 7 experiment. Nuclear data are usually produced from microscopic measures or theoretical models and are therefore characterised by uncertainties. These uncertainties lead to - sometimes large - propagated uncertainties on computed integral values.

The uncertainty calculation relies on two quantities, sensitivities and covariance matrices that describe the uncertainties on nuclear data. The uncertainty δR on the calculated values R can be therefore approximated through the "sandwich formula" [16]:

$$\delta R = \sqrt{{}^{t}SCS}$$

Where S is the sensitivity vector that gives the sensitivity of the calculated value to each cross section of each reaction, each isotope in each energy group, and C is the covariance matrix associated to the nuclear data evaluation.

As said before, the sensitivity vector has a direct and an indirect component that will be treated separately. The covariance matrix COMAC-v2.0 [18] is used for most isotopes. This covariance matrix is discretised on the ECCO-33 group energy mesh. However, some isotopes do not have covariance matrices in these libraries, such as both detectors and boron 11. Therefore, covariance matrices were generated using the NJOY [19] tool based on the ENDF/B-VIII.0 evaluation for the gold detector and the JEFF-3.2 evaluation for the sulphur detector as shown in Figure A 6. These evaluations have been used as they contain the required data to calculate the covariance matrices of the wanted reactions, in opposition to both COMAC-v2.0 and JEFF-3.1.1. For boron 11, two covariance matrices, based on the ENDF/B-VII.1 [20] and JENDL-4.0 [21] evaluations have been computed as shown in Figure A 5.

5.1. Direct effect

The uncertainty due to the direct effect requires the computation of the reaction rate in each energy group. First, the reaction rate on the 33-group energy mesh are presented in the positions presented in Figure 2 with red arrows, then the evolution of the uncertainty due to the direct effect is presented.

5.1.1. Gold detector

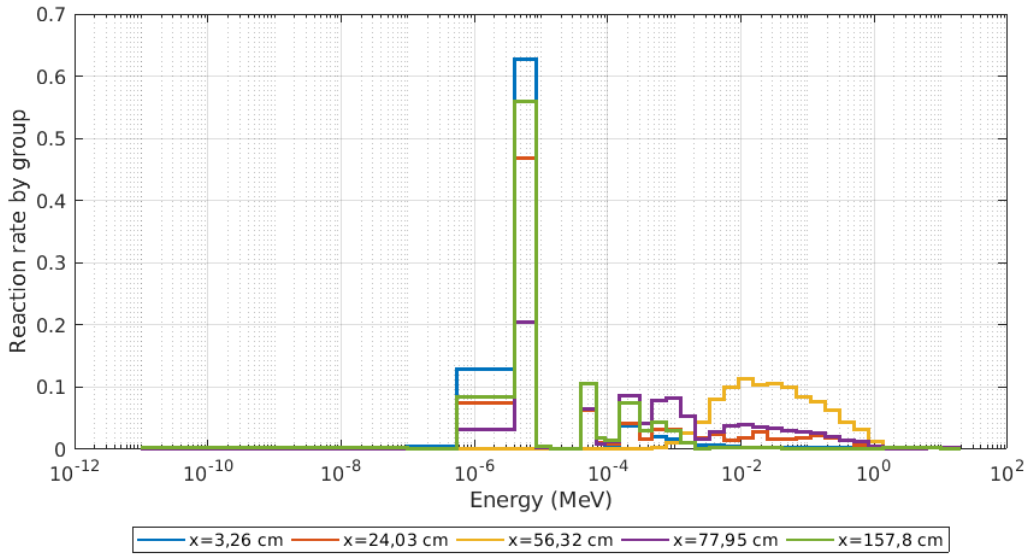

Figure 12. Evolution of the reaction rate by group for the gold detector

Figure 12 shows that with the exception of the detector inside the boron carbide zone (x=56.32 cm), most of the reaction rate occurs inside or around the gold resonance between 4 and 8 eV. For the detector inside the boron carbide (x=56.32 cm), almost the entire reaction rate happens for neutrons above 1 keV.

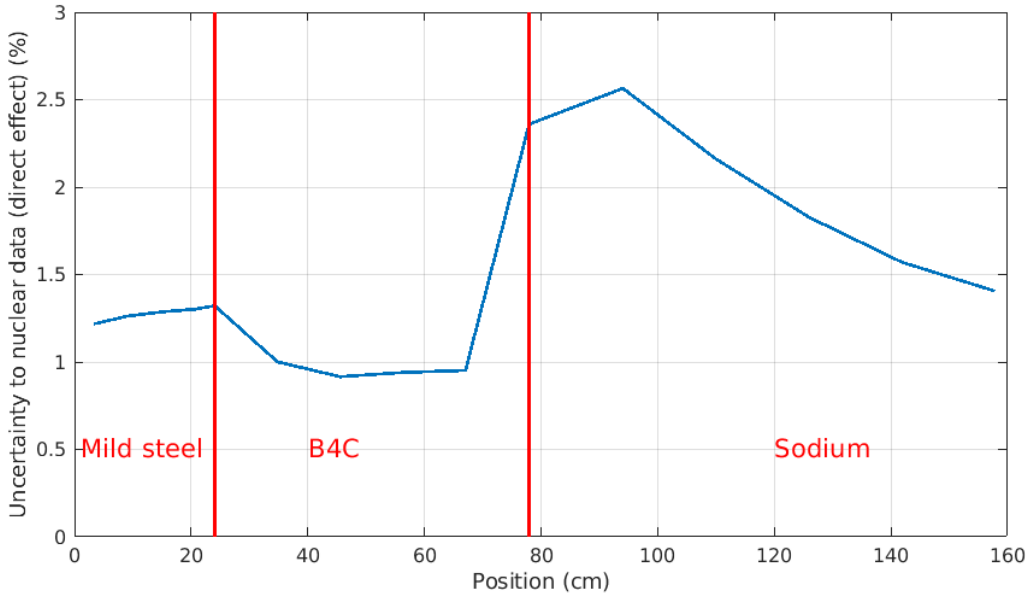

Figure 13. Evolution of the uncertainty due to nuclear data (gold detector, direct effect)

Figure 13 shows that the uncertainty due to the direct effect is very low for the gold detector and remains below 3 %. This is due to the low standard deviation of the gold radiative capture cross section in the ENDF/B-VIII.0 evaluation (Figure A 6).

5.1.2. Sulphur detector

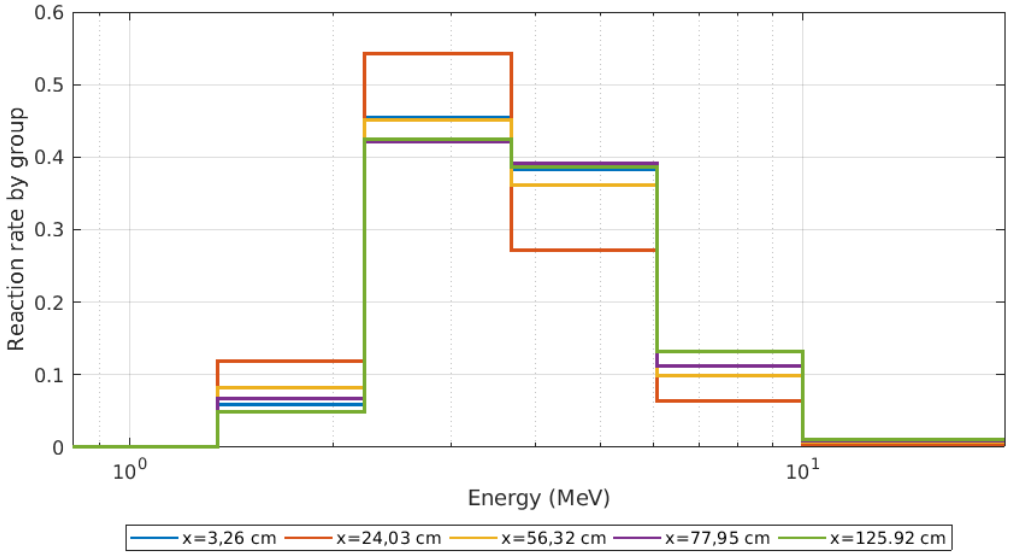

Figure 14. Evolution of the reaction rate by group for the sulphur detector

Figure 14 shows that the overall shape of the reaction rate remains similar during the propagation, with only a slight transfer to higher energies during propagation. The sensitivity in the lowest group remains low either.

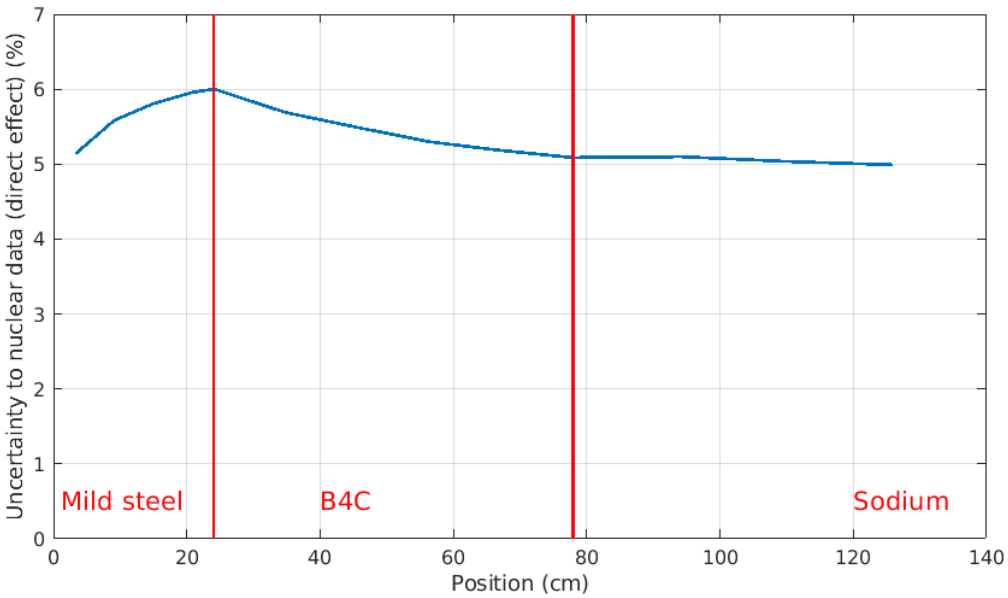

Figure 15. Evolution of the uncertainty due to nuclear data (sulphur detector, direct effect)

Figure 15 shows that the uncertainty due to the direct effect for the sulphur detector remains almost constant, with an average value around 5 %.

5.2. Indirect effect

As shown in section 4, some reactions have much higher sensitivity values than the others because of the abundance of the isotope or the impact of their cross section on the flux. Therefore, 33-group sensitivities for these reactions are computed while the other sensitivities are ignored.

5.2.1. Gold detector

The uncertainty due to each isotope is computed and presented below. As two covariance matrices were used for boron 11, the uncertainties obtained with both matrices are presented.

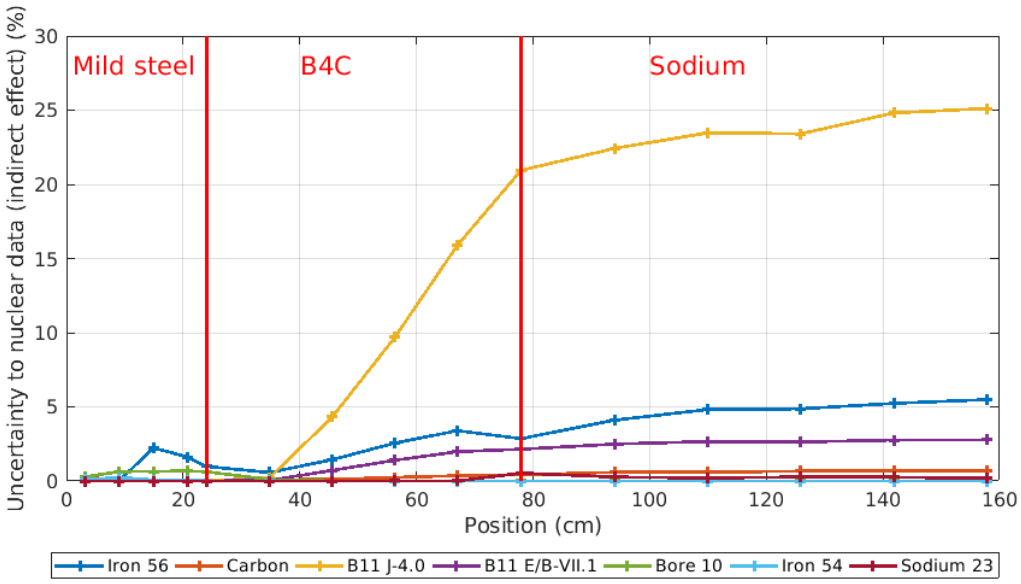

Figure 16. Uncertainty to nuclear data due to each isotope for the gold detector, indirect effect

Figure 16 shows that the two main isotopes that contribute to the uncertainty due to nuclear data are boron 11 and iron 56, the most common isotope in boron carbide and mild steel, respectively. This figure also shows that, in case of boron carbide, this uncertainty depends strongly on the covariance matrix used for the calculation, as the uncertainty computed with the JENDL-4.0 matrix is almost ten times the uncertainty computed with the ENDF/B-VII.1 matrix. This is due to the much higher standard deviation for elastic scattering provided in the first evaluation (Figure A 5). The total uncertainty to nuclear data will be computed using both matrices for boron 11, leading to somewhat different results.

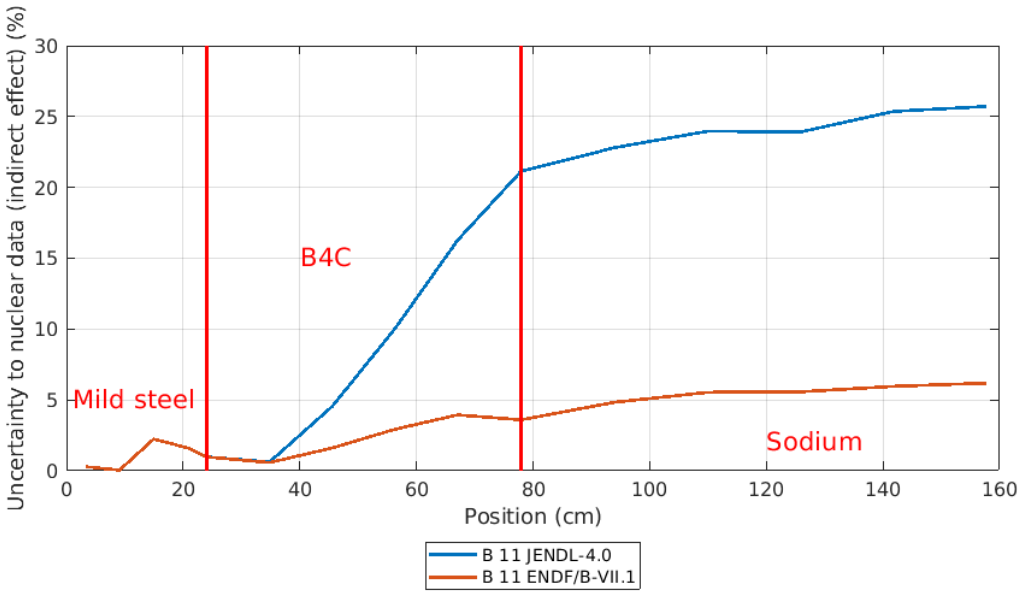

Figure 17. Evolution of the total uncertainty due to nuclear data (gold detector, indirect effect)

Figure 17 shows that the uncertainty due to the nuclear data indirect effect depends strongly on the covariance matrix used for the computation. The much higher propagated uncertainty from JENDL-4.0 is due to the combination of both a large standard deviation and the large sensitivity to the elastic scattering cross section of boron 11. The >20 % uncertainty calculated with JENDL-4.0 covers most of the biases between the calculation and the experiment except for the 10 % overestimation of the reaction rate at the beginning of the propagation.

5.2.2. Sulphur detector

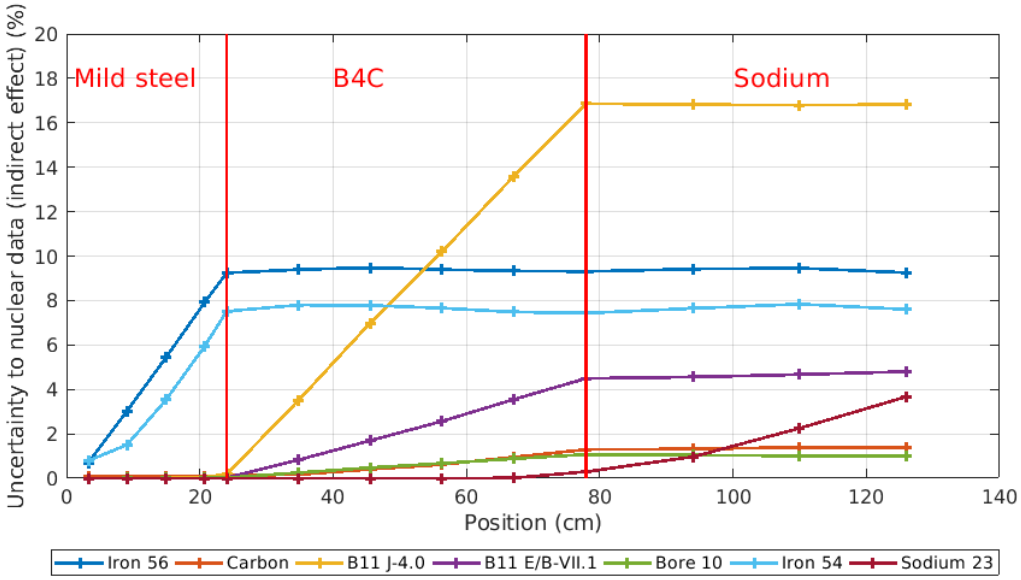

Figure 18. Uncertainty to nuclear data due to each isotope for the sulphur detector, indirect effect

Figure 18 shows that, as for the gold detector, boron 11 and iron 56 are among the largest contributors to the uncertainty due to nuclear data. However, in the case of the sulphur detector, the contributions

of iron 54 and sodium 23 are also not negligible. Most of the uncertainties are higher than for the gold detector, not only due to larger sensitivities but also because the highest sensitivities (elastic scattering of iron 56, boron 11 and sodium 23 for example) correspond to higher uncertainties above the sulphur threshold energys. The uncertainty due to boron 11 also depends closely on the covariance matrix used for this isotope even if the impact of the matrix is lower than in the case of the gold detector.

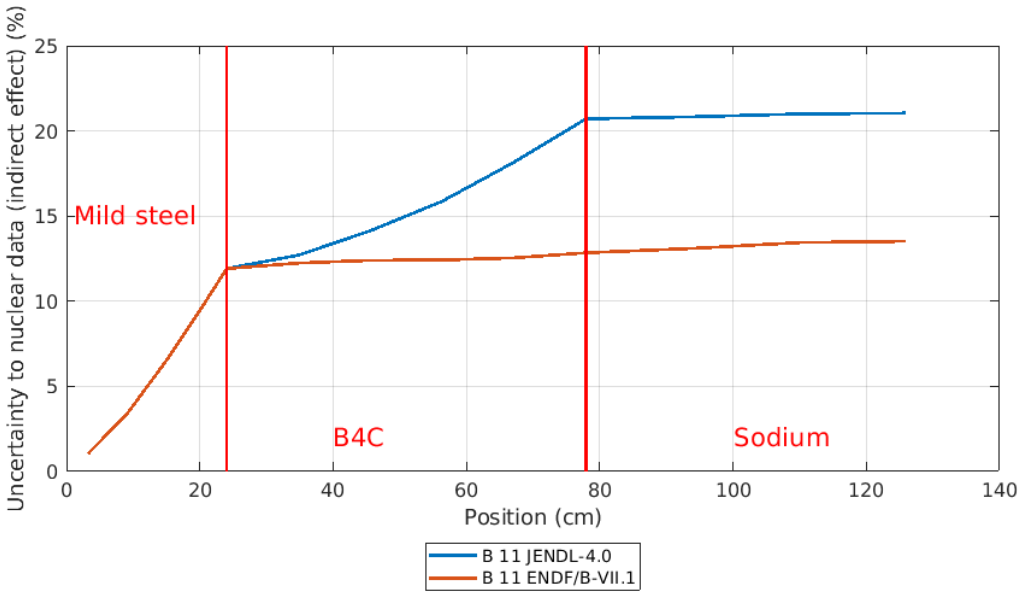

Figure 19. Evolution of the total uncertainty due to nuclear data (sulphur detector, indirect effect)

Figure 19 shows a similar behaviour to that obtained with the gold detector, with the JENDL-4.0 covariance matrix giving larger uncertainties than ENDF/B-VII.1, however with a smaller extent. Once again, the total propagated uncertainty calculated with the JENDL-4.0 covariance matrix can cover most of the observed biases, with the notable exception of the systematic underestimation at the beginning of the propagation.

5.3. Conclusion of the uncertainty calculations

The uncertainty calculations show that the impact of the indirect effect is much larger than the the one from direct effect for both gold and sulphur detectors. The indirect effect, is largely dependent to the covariance matric used for boron 11, which drives the largest sensitivities between all isotopes present in the geometry. The propagated uncertainties calculated with the JENDL-4.0 covariance matrix for boron 11 cover most of the JANUS Phase 7 C/E discrepancies obtained during the interpretation. Boron carbide being a thermal neutron absorber, it leads to the deep propagation of fast neutrons only. As uncertainties on nuclear data are usually higher for fast neutrons, it ends up with large uncertainties on all detector responses.

6. Conclusions

The interpretation of the JANUS Phase 7 SFR-like shielding experiment with the TRIPOLI-4® Monte Carlo code has been performed, using various nuclear data libraries for iron-56 evaluation. The interpretation shows that C/E discrepancies up to 20 % can be observed between the calculation and the experiment, with a strong dependency on the nuclear data of iron 56 and sodium, especially for

fast responses such as the sulphur detector. The C/E discrepancy is higher for ENDF/B-VIII.0, consistently to what was already observed in a previous ASPIS Iron 88 interpretation.

In order to understand these discrepancies, sensitivity calculations were performed using the correlated sampling method implemented in TRIPOLI-4®. These first of-a-kind calculations in the JANUS experiments show large sensitivities to the cross sections of the main isotopes in the geometry such as iron 56, boron 10 and 11 and sodium 23. Additional uncertainty calculations were performed based on these sensitivities. We showed a strong dependency on the covariance matrix used, in particular for boron 11. Coupling direct and indirect effects in the sensitivity analysis propagated uncertainties on calculated values give relatively large uncertainty values (up to 25 %). These values are of the same order of magnitude with the obtained C/E discrepancies.. Most of the uncertainty is brought by the indirect part, the direct part being responsible for only few percent at maximum, for either thermal or fast detector responses.

Overall, these studies show that precise neutron shielding calculations in materials such as boron carbide may represent a challenge for fast reactors. The physical phenomena involved (absorption of thermal neutrons leading to the propagation of fast neutrons, large uncertainties on nuclear data for fast energies) and the fact that some isotopes like boron 11 are usually not deeply considered for most nuclear core applications complexify the problem. Therefore, new evaluations with associated covariances are needed in order to design reliable neutron shielding using these materials. An extension of the combined Monte Carlo/S&U analysis to other NESTOR experiments should enrich and clarify the need to improve nuclear data for both thermal (ASPIS and NESDIP benchmarks [6]) and fast applications (JANUS 1 to 8 [3]).

7. References

[1] Beck, T., Chapoutier, N., Escleine, J. M., Gauthier, L., Occhipinti, D., Perrin, B., & Venard, C. (2018). Conceptual design of ASTRID radial shielding sub-assemblies. *Nuclear Engineering and Design*, 330, 129-137.

[2] Calamand, D., & Curl, I. J. (1990). A review of progress with the Janus programme of fast reactor shielding benchmark experiments. In *The physics of reactors: operation, design and computation. Volume 1*.

[3] Armishaw, M. J., Bryan, C. J., Calamand, D., Curl, I. J., Deadman, K., Hoare, C. J., Johnson, R. J., Locke, H. F., March, M. R., Murphy, M. F., Rickman, D. E. The JANUS Programme for fast reactor shielding. Experimental report, AEA Reactor Services.

[4] Hajji, A., Coquelet-Pascal, C., and Blaise, P. "Interpretation of the ASPIS Iron 88 programme with TRIPOLI-4® and quantification of uncertainties due to nuclear data." Annals of Nuclear Energy 140 (2020): 107147.

[5] Lefèvre, E. Mise au point et validation d'un nouveau formulaire adapté au calcul des protections neutroniques des réacteurs à neutrons rapides. PhD thesis, Aix-Marseille 1, 1996.

[6] Kodeli, I., Žerovnik, G., & Milocco, A. (2017). Examples of use of SINBAD database for nuclear data and code validation. In *EPJ Web of Conferences* (Vol. 153, p. 02010). EDP Sciences.

[7] Sartori, E., and Kodeli, I. Winfrith Iron Benchmark Experiment (ASPIS). SINBAD ABSTRACT NEA-1517/34.

[8] Brun, E., Damian, F., Diop, C. M., Dumonteil, E., Hugot, F. X., Jouanne, C. et al. (2014). TRIPOLI-4®, CEA, EDF and AREVA reference Monte Carlo code. In *SNA+ MC 2013-*

Joint International Conference on Supercomputing in Nuclear Applications+ Monte Carlo (p. 06023). EDP Sciences.

[9] Wright, G. A., Avery, A. F., Grimstone, M. J., Locke, H. F., & Newbon, S. (1994, April). Benchmarking of the JEF2. 2 Data library for Shielding Applications. In Proc. 8th ICRS.

[10] Santamarina, A., Bernard, D., Blaise, P., Coste, M., Courcelle, A., Huynh, TD., Jouanne, C., Leconte, P., Litaize, O., Mengelle, S. et al. The JEFF-3.1.1 nuclear data library. JEFF report, 22(10.2): 2, 2009.

[11] OECD Nuclear Energy Agency, *JEFF-3.2 Evaluated Data Library* (2014). http://www.oecd-nea.org/dbforms/data/eva/evatapes/jeff_32/

[12] Brown, DA., Chadwick, M. B., Capote, R., Kahler, A. C., Trkov, A., Herman, M. W., Sonzogni, A. A., Danon, Y., Carlson, A. D., Dunn, M. et al. ENDF/B-VIII.0: The 8th major release of the nuclear reaction data library with CIELO-project cross sections, new standards and thermal scattering data. Nuclear Data Sheets, 148: 1-142, 2018.

[13] Zsolnay EM, Capote Noy R., Nolthenius HJ, Trkov A (October 2014) International Reactor Dosimetry and Fusion File (IRDFF v1.05), https://nds.iaea.org/IRDFFv105/

[14] Sartori, E. Standard energy group structures of cross section libraries for reactor shielding, reactor cell and fusion neutronics applications: VITAMIN-J, ECCO-33, ECCO-2000 and XMAS. JEF/DOC-315, Revision, 3, 1990.

[15] Sublet, J-Ch., Packer, LW., Kopecky, J., Forrest, RA., Koning, AJ. and Rochman, DA. The European activation file: EAF-2010 neutron-induced cross section library. EASY Documentation Series, CCFE, 2010.

[16] Aliberti, G., Palmiotti, G., Salvatores, M., Kim, T. K., Taiwo, T. A., Anitescu, M., Tommasi, J., et al. (2006). Nuclear data sensitivity, uncertainty and target accuracy assessment for future nuclear systems. Annals of Nuclear Energy, 33(8), 700-733.

[17] Dejonghe, G., J. Gonnord, and J. C. Nimal. "Perturbation calculations by the correlated samples method." *Monte-Carlo Methods and Applications in Neutronics, Photonics and Statistical Physics*. Springer, Berlin, Heidelberg, 1985. 311-323.

[18] Archier, P., De Saint Jean, C., Noguere, G., Litaize, O., Leconte, P., & Bouret, C. (2015). *COMAC. Nuclear data covariance matrices library for reactor applications* (No. JAEA-CONF--2014-003).

[19] Macfarlane, R., Muir, D. W., Boicourt, R. M., Kahler III, A. C., & Conlin, J. L. (2017). *The NJOY Nuclear Data Processing System, Version 2016* (No. LA-UR-17-20093). Los Alamos National Lab.(LANL), Los Alamos, NM (United States).

[20] Chadwick, M. B., Herman, M., Obložinský, P., Dunn, M. E., Danon, Y., Kahler, A. C., ... & Brewer, R. (2011). ENDF/B-VII.1 nuclear data for science and technology: cross sections, covariances, fission product yields and decay data. *Nuclear data sheets*, *112*(12), 2887-2996.

[21] Shibata, K., Iwamoto, O., Nakagawa, T., Iwamoto, N., Ichihara, A., Kunieda, S., Chiba, S., Furutaka, K., Otuka, N., Ohsawa, T., et al. JENDL-4.0 : a new library for nuclear science and engineering. Journal of Nuclear Science and Technology, 48(1): 1-30, 2011.

8. Appendices

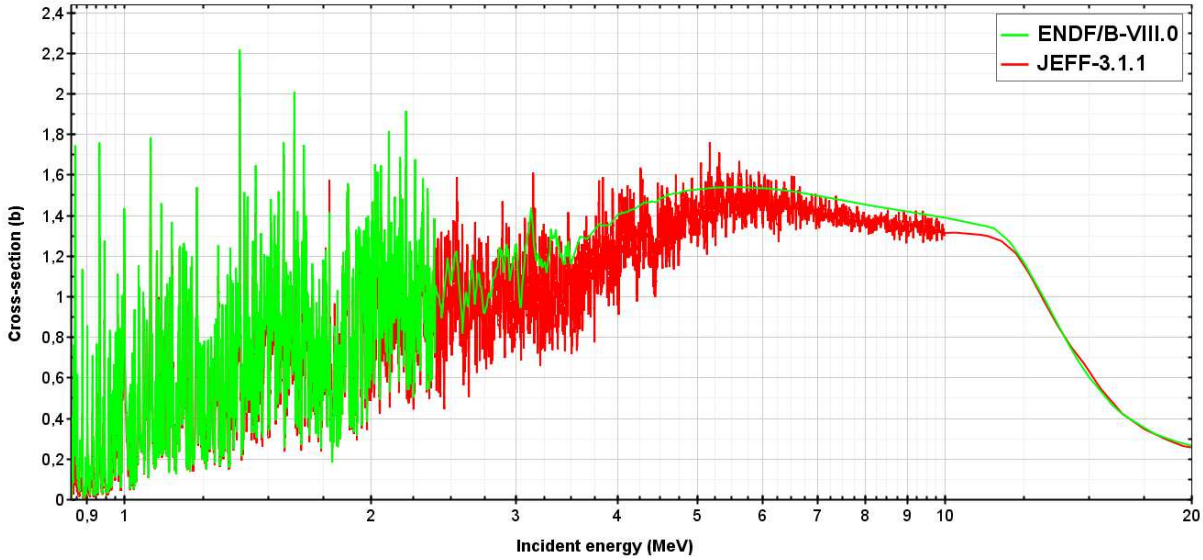

Figure A 1. Inelastic scattering cross section of iron 56

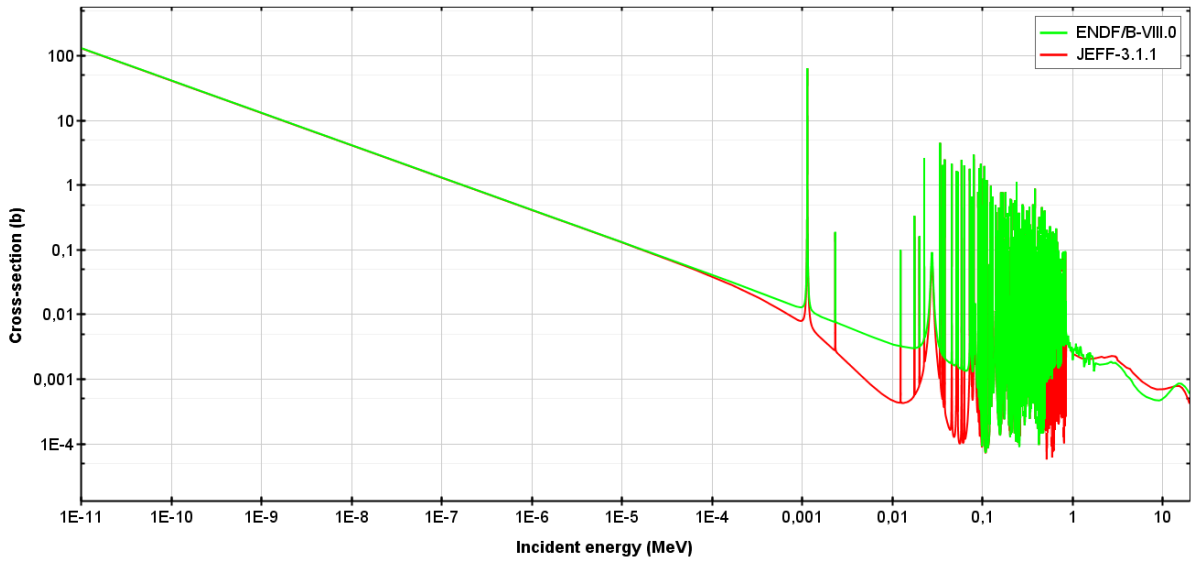

Figure A 2. Radiative capture cross section of iron 56

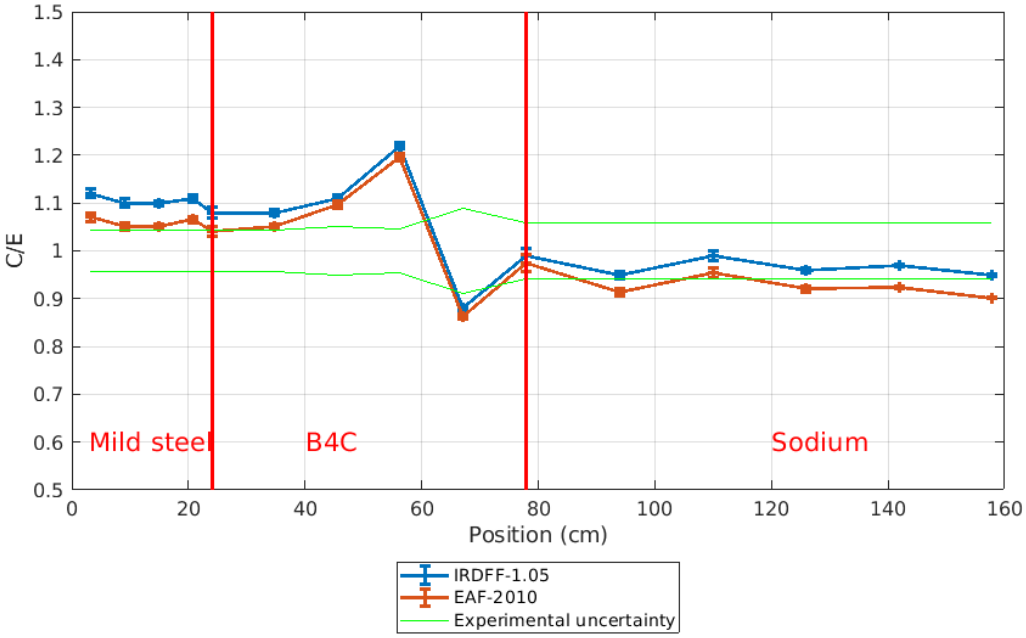

Figure A 3. Impact of the evaluation used for the gold detector (JEFF-3.1.1 used for neutron transport)

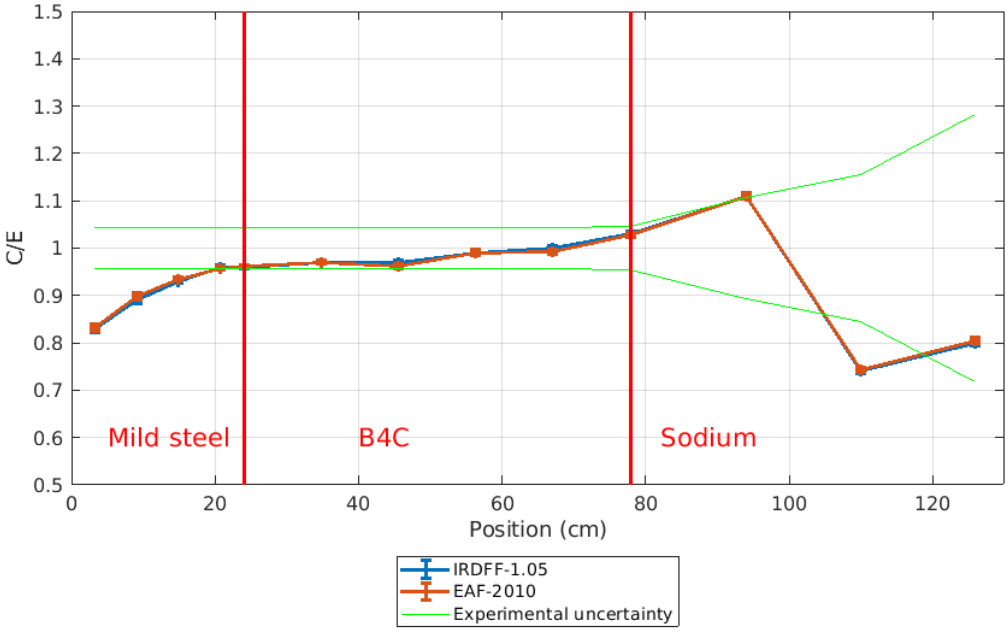

Figure A 4. . Impact of the evaluation used for the sulphur detector (JEFF-3.1.1 used for neutron transport)

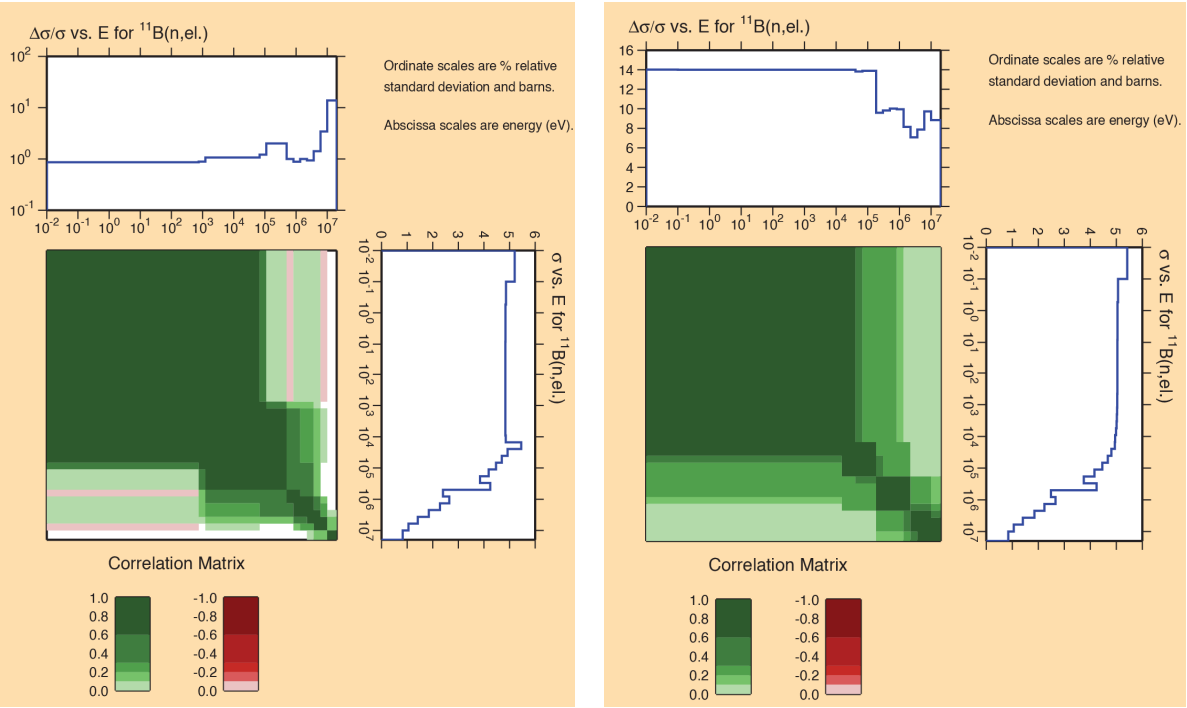

Figure A 5. Covariance matrices calculated for boron 11 : ENDF/B-VII.1 (left) and JENDL-4.0 (right)

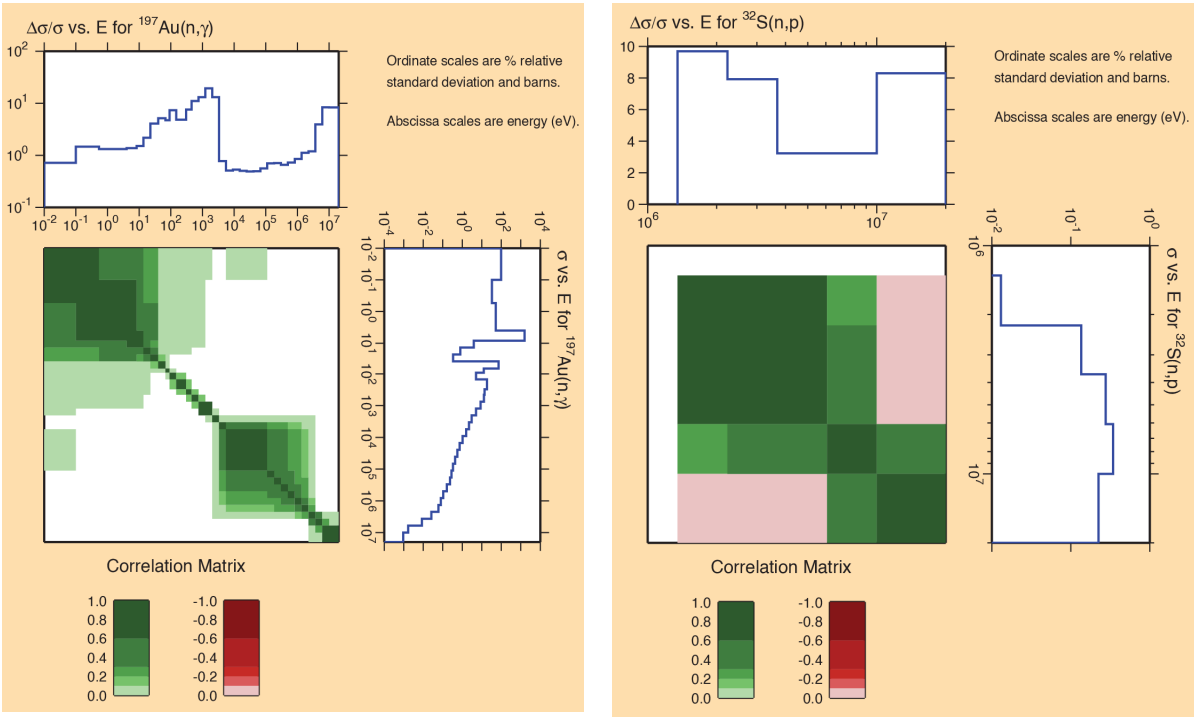

Figure A 6. Covariance matrices calculated for the detectors: gold (left) and sulphur (right)

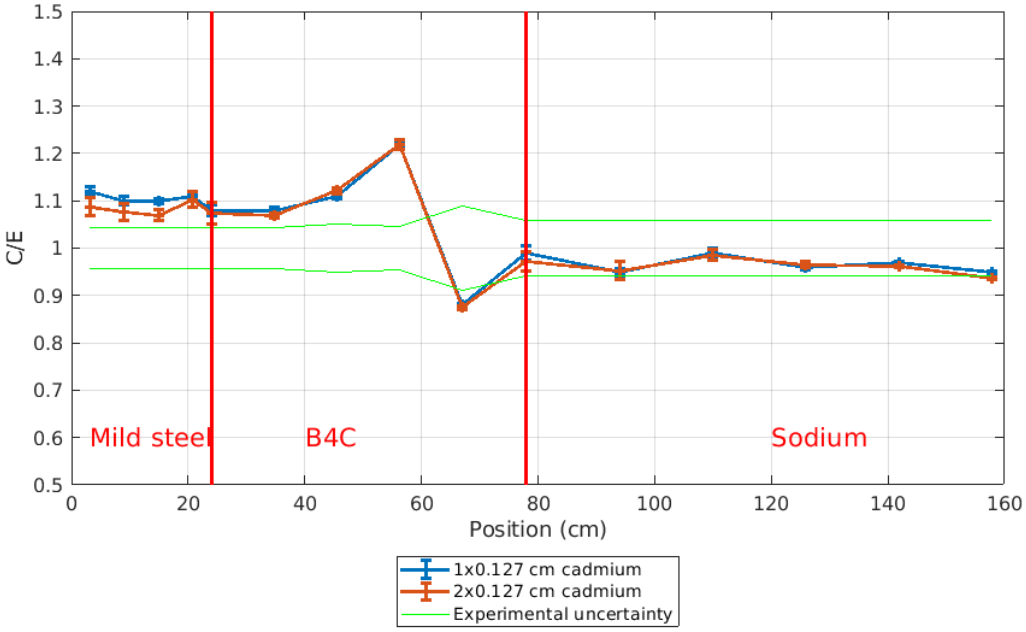

Figure A 7. Impact of the thickness used for the cadmium cover on the gold detector

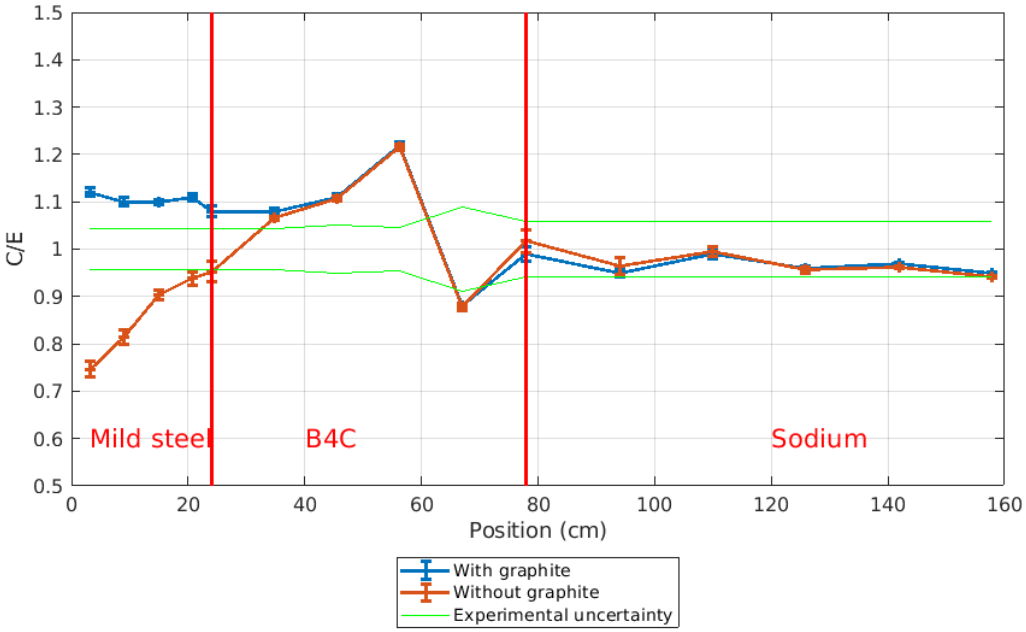

Figure A 8. Impact of the introduction of the graphite reflector on the reaction rates calculated for the gold detector

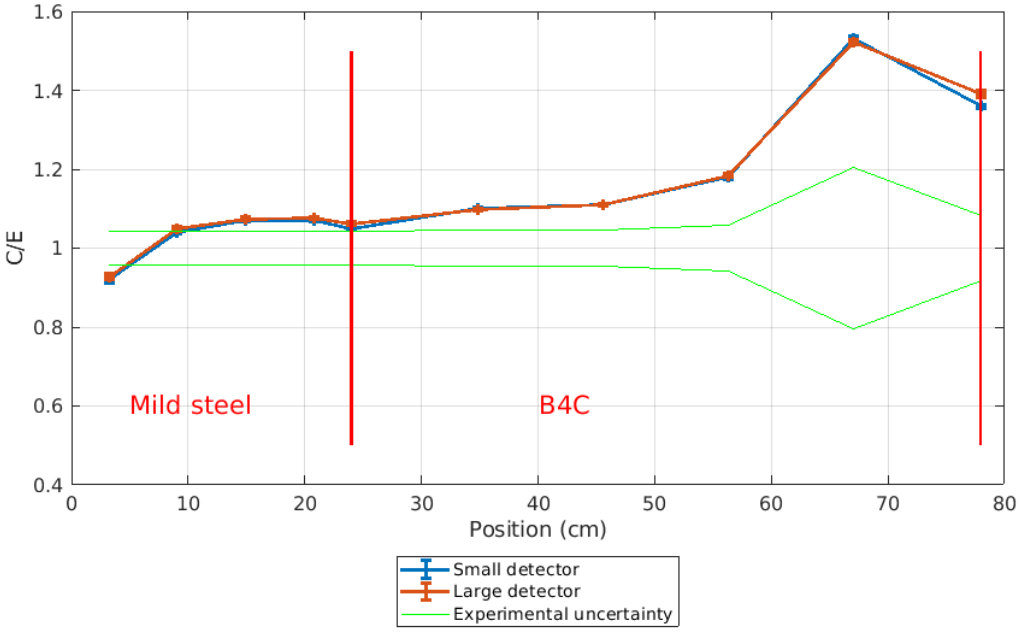

Figure A 9. Impact of the size of the rhodium detector

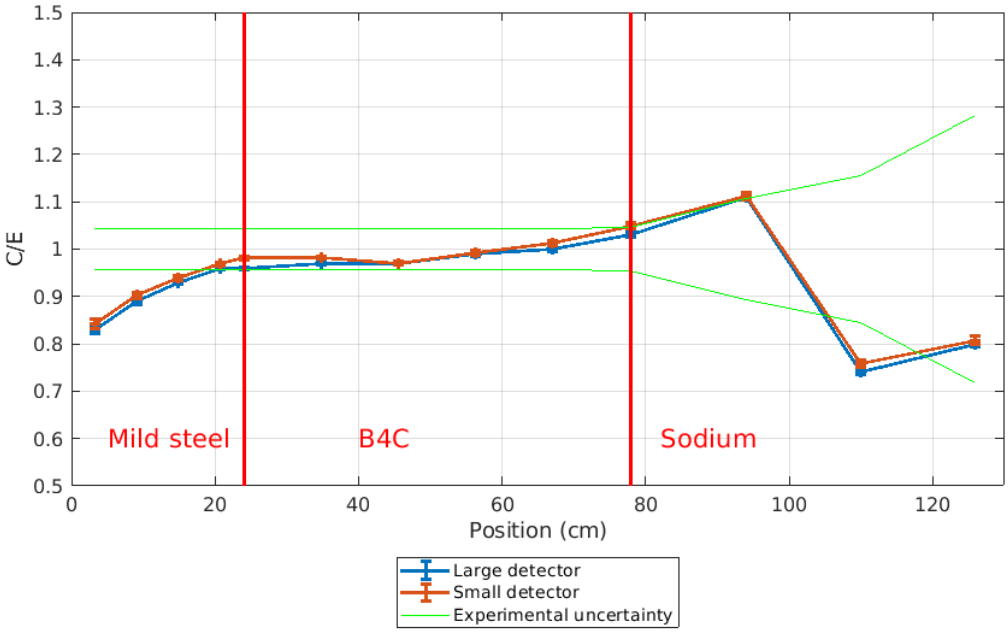

Figure A 10. Impact of the size of the sulphur detector